

Correlated insulator behaviour at half-filling in magic-angle graphene superlattices

Yuan Cao¹, Valla Fatemi¹, Ahmet Demir¹, Shiang Fang², Spencer L. Tomarken¹, Jason Y. Luo¹, Javier D. Sanchez-Yamagishi², Kenji Watanabe³, Takashi Taniguchi³, Efthimios Kaxiras^{2,4}, Ray C. Ashoori¹ & Pablo Jarillo-Herrero¹

A van der Waals heterostructure is a type of metamaterial that consists of vertically stacked two-dimensional building blocks held together by the van der Waals forces between the layers. This design means that the properties of van der Waals heterostructures can be engineered precisely, even more so than those of two-dimensional materials¹. One such property is the ‘twist’ angle between different layers in the heterostructure. This angle has a crucial role in the electronic properties of van der Waals heterostructures, but does not have a direct analogue in other types of heterostructure, such as semiconductors grown using molecular beam epitaxy. For small twist angles, the moiré pattern that is produced by the lattice misorientation between the two-dimensional layers creates long-range modulation of the stacking order. So far, studies of the effects of the twist angle in van der Waals heterostructures have concentrated mostly on heterostructures consisting of monolayer graphene on top of hexagonal boron nitride, which exhibit relatively weak interlayer interaction owing to the large bandgap in hexagonal boron nitride^{2–5}. Here we study a heterostructure consisting of bilayer graphene, in which the two graphene layers are twisted relative to each other by a certain angle. We show experimentally that, as predicted theoretically⁶, when this angle is close to the ‘magic’ angle the electronic band structure near zero Fermi energy becomes flat, owing to strong interlayer coupling. These flat bands exhibit insulating states at half-filling, which are not expected in the absence of correlations between electrons. We show that these correlated states at half-filling are consistent with Mott-like insulator states, which can arise from electrons being localized in the superlattice that is induced by the moiré pattern. These properties of magic-angle-twisted bilayer graphene heterostructures suggest that these materials could be used to study other exotic many-body quantum phases in two dimensions in the absence of a magnetic field. The accessibility of the flat bands through electrical tunability and the bandwidth tunability through the twist angle could pave the way towards more exotic correlated systems, such as unconventional superconductors and quantum spin liquids.

Exotic quantum phenomena, such as superconductivity and the fractional quantum Hall effect, often occur in condensed-matter systems and other systems with a high density of states. One way of creating a high density of states is to have ‘flat’ bands, which have weak dispersion in momentum space, with the kinetic energy of the electron set by the bandwidth W . When the Fermi level lies within the flat bands, Coulomb interactions (U) can greatly exceed the kinetic energy of the electrons and drive the system into various strongly correlated phases ($U/W \gg 1$)^{7–11}. The study of such flat-band systems in bulk materials is therefore scientifically important, and the search for new flat-band systems, such as in kagome and Lieb lattices and in heavy-fermion systems, is ongoing^{7–12}.

Recent advances in two-dimensional materials have provided a new route to achieving flat bands. An inherent advantage of two-dimensional materials is that the chemical potential of electrons can be tuned continuously via the electric-field effect without introducing extra disorder. In a twisted van der Waals heterostructure, the mismatch between two similar lattices generates a moiré pattern (Fig. 1b). This additional periodicity, which can have a length scale orders of magnitude larger than that of the underlying atomic lattices, has been shown to create a fractal energy spectrum in a strong magnetic field^{2–4}. In twisted layers, the interlayer hybridization is modulated by the moiré pattern as well. As an example, the band structure of twisted bilayer graphene (TBG) can be tailored to generate bandgaps and band curvatures that are otherwise absent^{6,13–17}. Although the well-known building blocks for van der Waals heterostructures, such as graphene and transition-metal dichalcogenides, do not have intrinsic flat bands at low energies, it has been predicted theoretically that flat bands could exist in TBG^{6,14–16,18}. Here we demonstrate experimentally that when the twist angle of TBG is close to the theoretically predicted magic angle, the interlayer hybridization induces nearly flat low-energy bands. This quenching of the quantum kinetic energy leads to a correlated insulating phase at half-filling of these flat bands, which is indicative of a Mott-like insulator in the localized flat bands.

To zeroth order, the low-energy band structure of TBG can be considered as two sets of monolayer-graphene Dirac cones rotated about the Γ point in the Brillouin zone by the twist angle θ (Fig. 1d)⁶. The difference between the two K (or K') wavevectors gives rise to the mini Brillouin zone (shown as a small hexagon), which is generated from the reciprocal lattice of the moiré superlattice (Fig. 1d). The Dirac cones near either the K or K' valley mix through interlayer hybridization, whereas interactions between distant Dirac cones are suppressed exponentially^{6,13}. As a result, the valley remains (for all practical purposes) a good quantum number. Two experimentally verified consequences of this hybridization are the energy gaps that open near the intersection of the Dirac cones and the renormalization of the Fermi velocity

$$v_F = \frac{1}{\hbar} |\nabla_k E_k|_{k=K,K'}$$

at the Dirac points^{13,19–21}.

The theoretically calculated magic angles $\theta_{\text{magic}}^{(i)}$, with $i = 1, 2, \dots$, are a series of twist angles at which the Fermi velocity at the Dirac points becomes zero⁶. The resulting low-energy bands near these twist angles are confined to less than about 10 meV. The flattening of the energy bands near the magic angle can be understood qualitatively from the competition between the kinetic energy and the interlayer hybridization energy (Fig. 1e–g). Intuitively, when the hybridization energy $2w$ is comparable to or larger than $\hbar v_0 k_\theta$, where $v_0 = 10^6 \text{ m s}^{-1}$ is the Fermi velocity of graphene, $k_\theta \approx G_K \theta$ is the momentum displacement of the

¹Department of Physics, Massachusetts Institute of Technology, Cambridge, Massachusetts 02139, USA. ²Department of Physics, Harvard University, Cambridge, Massachusetts 02138, USA. ³National Institute for Materials Science, Namiki 1-1, Tsukuba, Ibaraki 305-0044, Japan. ⁴John A. Paulson School of Engineering and Applied Sciences, Harvard University, Cambridge, Massachusetts 02138, USA.

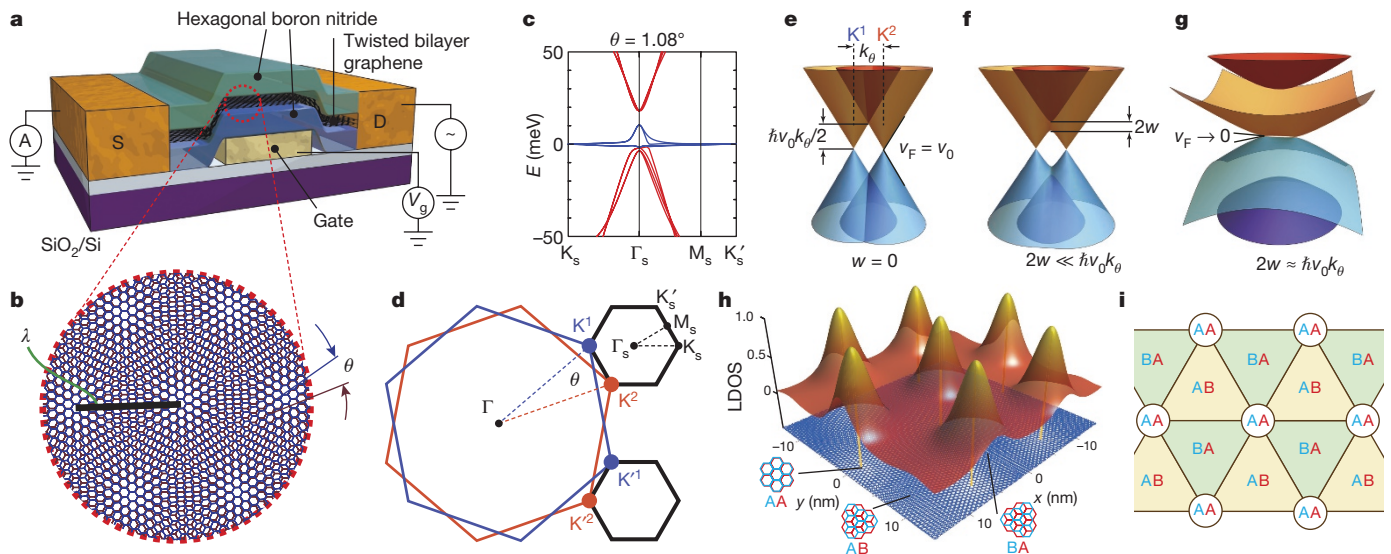


Figure 1 | Electronic band structure of twisted bilayer graphene (TBG). **a**, Schematic of the TBG devices. The TBG is encapsulated in hexagonal boron nitride flakes with thicknesses of about 10–30 nm. The devices are fabricated on SiO₂/Si substrates. The conductance is measured with a voltage bias of 100 μ V while varying the local bottom gate voltage V_g . ‘S’ and ‘D’ are the source and drain contacts, respectively. **b**, The moiré pattern as seen in TBG. The moiré wavelength is $\lambda = a/[2\sin(\theta/2)]$, where $a = 0.246$ nm is the lattice constant of graphene and θ is the twist angle. **c**, The band energy E of magic-angle ($\theta = 1.08^\circ$) TBG calculated using an *ab initio* tight-binding method. The bands shown in blue are the flat bands that we study. **d**, The mini Brillouin zone is constructed from the difference between the two K (or K’) wavevectors for the two layers.

Dirac cones, $G_K = 4\pi/(3\alpha)$ is the magnitude of the wavevector Γ –K of graphene, $\alpha = 0.246$ nm is the lattice constant of graphene and $\hbar = h/(2\pi)$ is the reduced Planck constant, the lower of the hybridized states is pushed to and crosses zero energy. A mathematical derivation of the magic-angle condition⁶ gives the first magic angle, $\theta_{\text{magic}}^{(1)} = \sqrt{3}w/(\hbar v_0 G_K) \approx 1.1^\circ$. In Fig. 1c we show an *ab initio* tight-binding calculation¹⁶ of the band structure for $\theta = 1.08^\circ$. The flat bands (coloured blue) have a bandwidth of 12 meV for the $E > 0$ branch and 2 meV for the $E < 0$ branch (where E is the band energy). From a band-theory point of view, the flat bands should have localized wavefunction profiles in real space. In Fig. 1h we show the local density of states calculated for the flat bands. The wavefunctions are indeed highly concentrated in the regions with AA stacking, whereas small but non-zero amplitudes on the AB and BA regions connect the AA regions and endow the bands with weak dispersion^{6,15,18}. A brief discussion about the topological structure of the bands near the first magic angle is given in Methods and Extended Data Fig. 1.

For the experiment, we fabricated high-quality encapsulated TBG devices with the twist angle controlled to an accuracy of about 0.1° – 0.2° using a previously developed ‘tear and stack’ technique^{13,17,22}. We measured four devices with twist angles near the first magic angle $\theta_{\text{magic}}^{(1)} \approx 1.1^\circ$. In Fig. 2a we show the low-temperature two-probe conductance of device D1 as a function of carrier density n . For $n \approx \pm n_s = \pm 2.7 \times 10^{12} \text{ cm}^{-2}$ (four electrons per moiré unit cell for $\theta = 1.08^\circ$), the conductance is zero over a wide range of densities. Here, n_s refers to the density that is required to fill the mini Brillouin zone, accounting for spin and valley degeneracies (see Methods). These insulating states have been explained previously as hybridization-induced bandgaps above and below the lowest-energy superlattice bands, and are hereafter referred to as ‘superlattice gaps’¹³. The thermal activation gaps are measured to be about 40 meV (see Methods)^{13,17}. The twist angle can be estimated from the density that is required to reach the superlattice gaps, which we find to be $\theta = 1.1^\circ \pm 0.1^\circ$ for all of the devices reported here.

Hybridization occurs between Dirac cones within each valley, whereas intervalley processes are strongly suppressed. K_s, K'_s, M_s and Γ_s denote points in the mini Brillouin zone. **e–g**, Illustration of the effect of interlayer hybridization for $w = 0$ (**e**), $2w \ll \hbar v_0 k_\theta$ (**f**) and $2w \approx \hbar v_0 k_\theta$ (**g**); $v_0 = 10^6 \text{ m s}^{-1}$ is the Fermi velocity of graphene. **h**, Normalized local density of states (LDOS) calculated for the flat bands with $E > 0$ at $\theta = 1.08^\circ$. The electron density is strongly concentrated at the regions with AA stacking order, whereas it is mostly depleted at AB- and BA-stacked regions. See Extended Data Fig. 6 for the density of states versus energy at the same twist angle. **i**, Top view of a simplified model of the stacking order.

Another pair of insulating states occurs for a narrower density range, near half the superlattice density: $n \approx \pm n_s/2 = \pm 1.4 \times 10^{12} \text{ cm}^{-2}$ (two electrons per moiré unit cell). These insulating states have a much smaller energy scale. This behaviour is markedly different from all other zero-field insulating behaviours reported previously, which occur at integer multiples of $\pm n_s$ (refs 13, 17). We refer to the states that occur near $\pm n_s/2$ as ‘half-filling insulating states’. They are observed at roughly the same density for all four devices (Fig. 2a, inset). In Fig. 2b–d we show the conductance of the half-filling states in device D1 at different temperatures. Above 4 K, the system behaves as a metal, exhibiting decreasing conductance with increasing temperature. A metal–insulator transition occurs at around 4 K. The conductance drops substantially from 4 K to 0.3 K, with the minimum value decreasing by 1.5 orders of magnitude. An Arrhenius fit yields a thermal activation gap of about 0.3 meV for the half-filling states, two orders of magnitude smaller than those of the superlattice gaps. At the lowest temperatures, the system can be limited by conduction through charge puddles, resulting in deviation from the Arrhenius fit.

To confirm the existence of the half-filling states, we performed capacitance measurements on device D2 using an a.c. low-temperature capacitance bridge (Extended Data Fig. 2)²³. The real and imaginary components of the a.c. measurement provide information about the change in capacitance and the loss tangent of the device, respectively. The latter signal is tied to the dissipation in the device due to its resistance²³. Device D2 exhibits a reduction in capacitance and strong enhancement of dissipation at $\pm n_s/2$ (Fig. 3a), in agreement with an insulating phase that results from the suppression of the density of states. The insulating state at $-n_s/2$ is weaker and visible only in the dissipation data. The observation of capacitance reduction (that is, suppression of density of states) for only the n-side half-filling state in this device may be due to an asymmetric band structure or the quality of the device. The reduction (enhancement) in capacitance (dissipation) vanishes when the device is warmed up from 0.3 K to about 2 K, consistent with the behaviour observed in transport measurements.

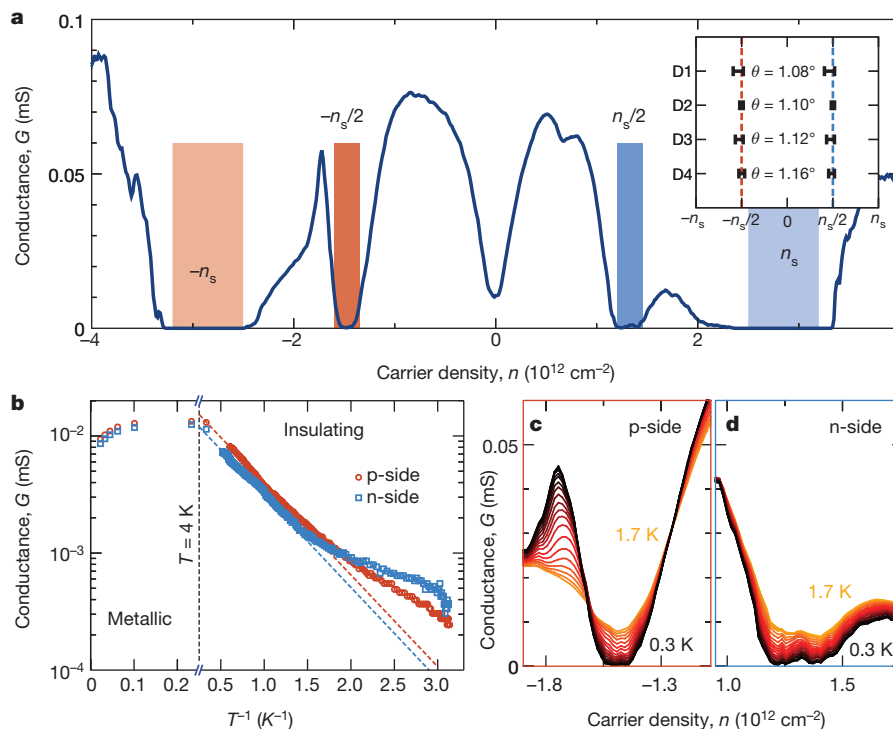


Figure 2 | Half-filling insulating states in magic-angle TBG. **a**, Measured conductance G of magic-angle TBG device D1 with $\theta = 1.08^\circ$ and $T = 0.3$ K. The Dirac point is located at $n = 0$. The lighter-shaded regions are superlattice gaps at carrier density $n = \pm n_s = \pm 2.7 \times 10^{12} \text{ cm}^{-2}$. The darker-shaded regions denote half-filling states at $\pm n_s/2$. The inset shows the density locations of half-filling states in the four different devices.

The emergence of half-filling states is not expected in the absence of interactions between electrons and appears to be correlated with the narrow bandwidth near the first magic angle. In our experiment, several separate pieces of evidence support the presence of flat bands. First, we measured the temperature dependence of the amplitude of Shubnikov–de Haas oscillations in device D1, from which we extracted the effective mass of the electron, m^* (Fig. 3b; see Methods and Extended Data Fig. 3 for analysis). For a Dirac spectrum with eight-fold degeneracy (spin, valley and layer), we expect that $m^* = \sqrt{\hbar^2 n / (8\pi v_F^2)}$, which scales as $1/v_F$. The large measured m^* near charge neutrality in device D1 indicates a reduction in v_F by a factor of 25 compared to monolayer graphene ($4 \times 10^4 \text{ m s}^{-1}$ compared to 10^6 m s^{-1}). This large reduction in the Fermi velocity is a characteristic that is expected for flat bands. Second, we analysed the capacitance data of device D2 near the Dirac point (Fig. 3a) and found that v_F needs to be reduced to about $0.15v_0$ for a good fit to the data (Methods, Extended Data Fig. 1b). Third, another direct manifestation of flat bands is the flattening of the conductance minimum at charge neutrality above a temperature of 40 K (thermal energy $kT = 3.5 \text{ meV}$), as seen in Fig. 3c. Although the conductance minimum in monolayer graphene can be observed clearly even near room temperature, it is smeared out in magic-angle TBG when the thermal energy kT becomes comparable to $v_F \hbar / 2 \approx 4 \text{ meV}$ —the energy scale that spans the Dirac-like portion of the band (Fig. 1c)^{24–26}.

Owing to the localized nature of the electrons, a plausible explanation for the gapped behaviour at half-filling is the formation of a Mott-like insulator driven by Coulomb interactions between electrons^{27,28}. To this end, we consider a Hubbard model on a triangular lattice, with each site corresponding to a localized region with AA stacking in the moiré pattern (Fig. 1i). In Fig. 3d we show the bandwidth of the $E > 0$ branch of the low-energy bands for $0.04^\circ < \theta < 2^\circ$ that we calculated numerically using a continuum model of TBG⁶. The bandwidth W is strongly suppressed near the magic angles. The on-site Coulomb energy U of each site is estimated to be $e^2 / (4\pi\epsilon d)$, where d is the effective linear

See Methods for a definition of the error bars. **b**, Minimum conductance values in the p-side (red) and n-side (blue) half-filling states in device D1. The dashed lines are fits of $\exp[-\Delta/(2kT)]$ to the data, where $\Delta \approx 0.31 \text{ meV}$ is the thermal activation gap. **c**, **d**, Temperature-dependent conductance of D1 for temperatures from about 0.3 K (black) to 1.7 K (orange) near the p-side (**c**) and n-side (**d**) half-filling states.

dimension of each site (with the same length scale as the moiré period), ϵ is the effective dielectric constant including screening and e is the electron charge. Combining ϵ and the dependence of d on twist angle into a single constant κ , we write $U = e^2 \theta / (4\pi\epsilon_0 \kappa a)$, where $a = 0.246 \text{ nm}$ is the lattice constant of monolayer graphene. In Fig. 3d we plot the on-site energy U versus θ for $\kappa = 4–20$. As a reference, $\kappa = 4$ if we assume $\epsilon = 10\epsilon_0$ and d is 40% of the moiré wavelength. For a range of possible values of κ it is therefore reasonable that $U/W > 1$ occurs near the magic angles and results in half-filling Mott-like gaps²⁷. However, the realistic scenario is much more complicated than these simplistic estimates; a complete understanding requires detailed theoretical analyses of the interactions responsible for the correlated gaps.

The Shubnikov–de Haas oscillation frequency f_{SDH} (Fig. 3b) also supports the existence of Mott-like correlated gaps at half-filling. Near the charge neutrality point, the oscillation frequency closely follows $f_{\text{SDH}} = \phi_0 |n| / M$ where $\phi_0 = h/e$ is the flux quantum and $M = 4$ indicates the spin and valley degeneracies. However, at $|n| > n_s/2$, we observe oscillation frequencies that corresponds to straight lines, $f_{\text{SDH}} = \phi_0 (|n| - n_s/2) / M$, in which M has a reduced value of 2. Moreover, these lines extrapolate to zero exactly at the densities of the half-filling states, $n = \pm n_s/2$. These oscillations point to small Fermi pockets that result from doping the half-filling states, which might originate from charged quasiparticles near a Mott-like insulator phase²⁹. The halved degeneracy of the Fermi pockets might be related to the spin–charge separation that is predicted in a Mott insulator²⁹. These results are also supported by Hall measurements at 0.3 K (Extended Data Fig. 4; see Methods for discussion), which show a ‘resetting’ of the Hall densities when the system is electrostatically doped beyond the Mott-like states.

The half-filling states at $\pm n_s/2$ are suppressed by the application of a magnetic field. In Fig. 4a, b we show that both insulating phases start to conduct at a perpendicular field of $B = 4 \text{ T}$ and recover normal conductance by $B = 8 \text{ T}$. A similar effect is observed for an in-plane magnetic field (Extended Data Fig. 5d). The insensitivity to field

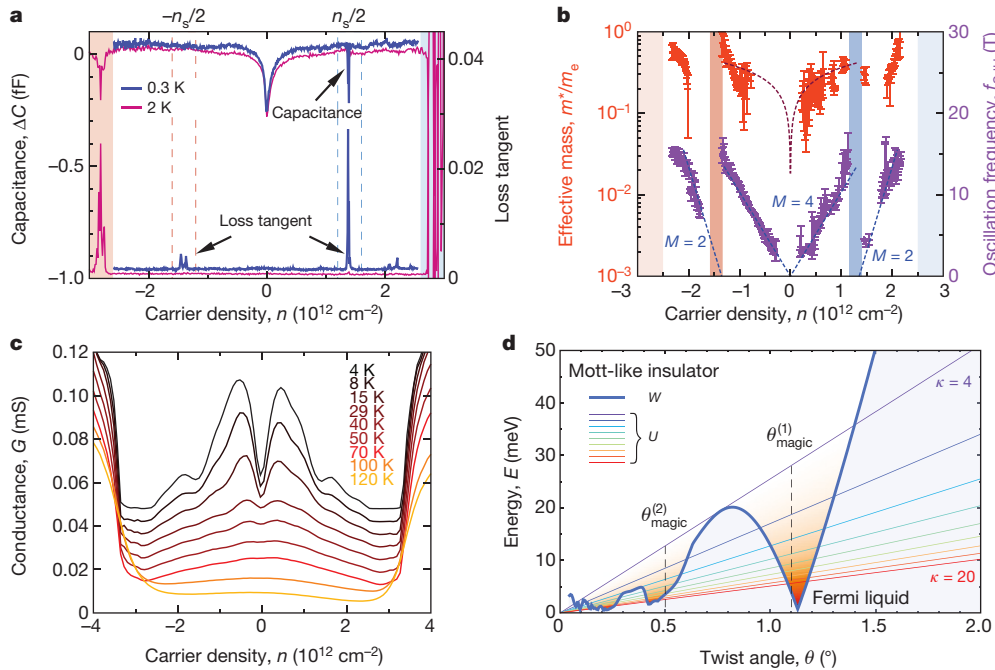


Figure 3 | Flat bands in magic-angle TBG. **a**, Capacitance measurements of device D2 at 0.3 K (blue) and 2 K (pink). The change in the measured capacitance (ΔC ; upper traces) is plotted on the left axis and the loss tangent (lower traces) is shown on the right axis. For densities corresponding to half-filling ($\pm n_s/2$; dashed vertical lines), a reduction in ΔC (on the p-side only) and an enhancement in loss tangent (on both sides) are observed in the 0.3 K data. These effects disappear in the 2 K measurements. **b**, The effective mass m^* and oscillation frequency f_{sdH} as extracted from temperature-dependent Shubnikov–de Haas oscillations. The fitting curve (red dashed line) is $m^* = \sqrt{h^2|n|/(8\pi v_F^2)}$, assuming a uniform Fermi velocity of v_F . For magic-angle device D1, the estimated Fermi velocity of $v_F = 4 \times 10^4 \text{ m s}^{-1}$ is a factor of 25 less than that for pristine graphene, $v_0 = 10^6 \text{ m s}^{-1}$. The measured oscillation frequencies indicate the existence of small Fermi pockets that start from the half-filling states, with half the degeneracy of the main Fermi surface of the Dirac points. Shaded regions at half-filling and full-filling correspond to the

shaded rectangles in Fig. 2a. The error bars in m^* and f_{sdH} give the uncertainty of fitting to the Lifshitz–Kosevich formula (defined in Methods) and correspond to the 90% confidence level. The blue dashed curves denote the f_{sdH} that is expected for Fermi surfaces with degeneracy $M = 4$ and $M = 2$, starting at charge neutrality and at the half-filling states, respectively. **c**, Gate dependence of the conductance of device D1 at different temperatures, 4.5 K, 8 K, 15 K, 29 K, 40 K, 50 K, 70 K, 100 K and 120 K. The curves are each shifted vertically by 0.006 mS for clarity. See Extended Data Fig. 5a, b for the temperature dependence up to room temperature. **d**, Comparison between the bandwidth W for the $E > 0$ flat-band branch in TBG (thick blue line) and the on-site energy $U = e^2\theta/(4\pi\epsilon_0\kappa a)$ (thin coloured lines for different values of κ) for different twist angles θ . Near the magic angles $\theta_{\text{magic}}^{(i)} \approx 1.1^\circ, 0.5^\circ, \dots$ for $i = 1, 2, \dots$, $U > W$ is satisfied for a range of possible values of κ (defined in the main text) and so the system can be driven into a Mott-like insulator state.

orientation suggests that the suppression of the half-filling states is due to a Zeeman effect rather than an orbital effect, because the latter would be affected by only the perpendicular component of the magnetic field. For an effective g -factor of $g = 2$ due to electron

spin, the Zeeman energy that is needed to suppress the half-filling states is approximately $g\mu_B B = 0.5 \text{ meV}$, where μ_B is the Bohr magneton—the same order of magnitude as that of the thermal excitation energy.

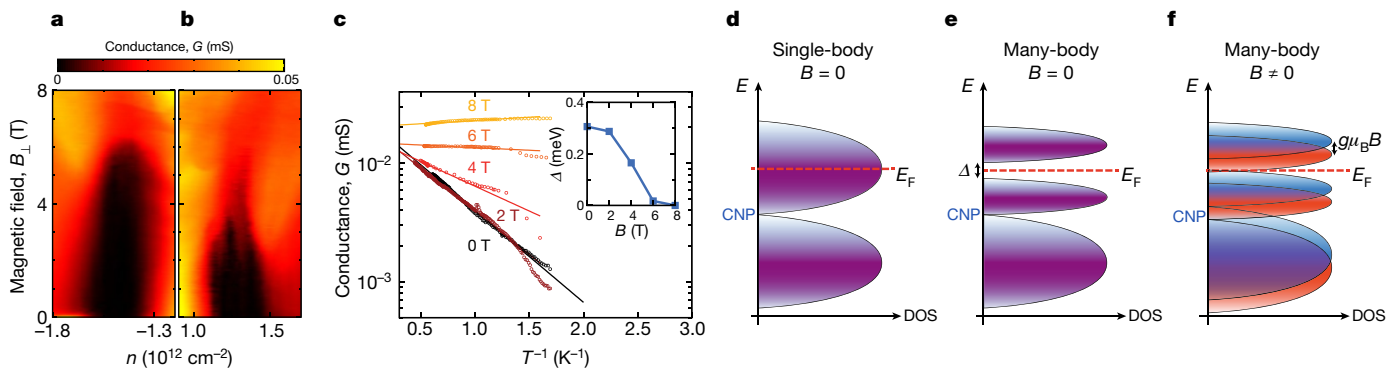


Figure 4 | Magnetic-field response of the half-filling insulating phases. **a**, **b**, Dependence of the conductance on the perpendicular magnetic field B_\perp of the half-filling states for device D1 on the p-side (**a**) and the n-side (**b**). The measurement is taken at 0.3 K. **c**, Arrhenius plot (circles) of the conductance of the p-side half-filling state at different magnetic fields. The inset shows the thermal activation gap Δ extracted from fitting the data in the main plot with $\exp[-\Delta/(2kT)]$ (solid lines). **d–f**, Schematics of the density of states (DOS) in different scenarios. The single-particle flat bands ($E > 0$ and $E < 0$ bands are both shown, with E_F in the $E > 0$

band (n -doping); **d**) are split into upper and lower many-body bands by interactions (**e**). This occurs when E_F is at half-filling of the upper band. Upon applying a Zeeman field ($B \neq 0$), the excitations can be further polarized, and can close the charge gap when the Zeeman energy $g\mu_B B$ is comparable to the gap Δ (**f**). Purple shading denotes a spin-degenerate band, whereas blue and red shading denotes spin-up and spin-down bands, respectively. CNP, charge neutrality point. The shape of the DOS drawn here is purely illustrative and does not represent the actual DOS profile (see Extended Data Fig. 6 for a numerical result).

Our data point to the presence of a spin-singlet Mott-like insulator ground state at half-filling and zero magnetic field (Fig. 4e). The application of an external magnetic field could polarize the excitations in the spectrum of the correlated states according to their spin. When the Zeeman energy exceeds the charge gap, charge conduction can therefore occur (Fig. 4f). In a typical Mott insulator, the ground state usually exhibits antiferromagnetic spin ordering below the Néel temperature. However, on a triangular lattice, the frustration prevents fully antiparallel alignment of adjacent spins. Possible ordering schemes include the 120° Néel order and a rotational-symmetry-breaking stripe order³⁰. It is unclear whether the spin-singlet ground state in magic-angle TBG is fulfilled by either of these ordering schemes, or whether it is disordered at low temperatures. In the half-filling states of magic-angle TBG it is also possible that the ordering, if any, occurs in conjunction with the valley degree of freedom. Therefore, any complete theoretical treatment of this problem should include a two-band Hubbard model on a triangular lattice.

We also comment on other competing mechanisms for creating a half-filled insulating state in a system with flat bands. Among the possibilities, charge-density waves in two dimensions are often stabilized by Fermi-surface nesting, which can in principle occur near the half-filling of a two-dimensional Brillouin zone³¹. However, this nesting is not sufficient to create a global gap in the entire Fermi surface to achieve an insulating state. To create a global gap at half-filling, at least a doubling of the unit cell would be necessary, which could be created by a commensurate charge-density wave or lattice relaxation due to strain. Scanning tunnelling microscopy conducted at temperatures below 4 K may be able to differentiate such mechanisms.

In summary, our work demonstrates that graphene can be transformed through van der Waals engineering into a flat-band system in which insulating states at half-filling are present. These insulating states cannot be explained in the absence of electron–electron interactions and so highlight the importance of correlations in this flat-band system. However, the lattice and electronic structure near magic-angle TBG superlattices is very complex, and further theoretical and experimental work is necessary to ascertain the importance of correlation effects fully. Through its easy gate tunability, magic-angle TBG could provide a way of studying the transition between a correlated metal and an interaction-driven insulating state, which could provide insights into strongly correlated materials, including high-temperature superconductivity. The combination of spin and valley degrees of freedom on a triangular lattice could also give rise to other exotic quantum phases, such as quantum spin liquids³².

Online Content Methods, along with any additional Extended Data display items and Source Data, are available in the online version of the paper; references unique to these sections appear only in the online paper.

Received 6 October 2017; accepted 21 February 2018.

Published online 5 March 2018.

- Geim, A. K. & Grigorieva, I. V. Van der Waals heterostructures. *Nature* **499**, 419–425 (2013).
- Hunt, B. *et al.* Massive Dirac fermions and Hofstadter butterfly in a van der Waals heterostructure. *Science* **340**, 1427–1430 (2013).
- Dean, C. R. *et al.* Hofstadter's butterfly and the fractal quantum Hall effect in moiré superlattices. *Nature* **497**, 598–602 (2013).
- Ponomarenko, L. A. *et al.* Cloning of Dirac fermions in graphene superlattices. *Nature* **497**, 594–597 (2013).
- Song, J. C. W., Shytov, A. V. & Levitov, L. S. Electron interactions and gap opening in graphene superlattices. *Phys. Rev. Lett.* **111**, 266801 (2013).
- Bistrizter, R. & MacDonald, A. H. Moiré bands in twisted double-layer graphene. *Proc. Natl Acad. Sci. USA* **108**, 12233–12237 (2011).
- Wu, C., Bergman, D., Balents, L. & Das Sarma, S. Flat bands and Wigner crystallization in the honeycomb optical lattice. *Phys. Rev. Lett.* **99**, 070401 (2007).
- Iglovikov, V. I., Hèbert, F., Grèmaud, B., Batrouni, G. G. & Scalettar, R. T. Superconducting transitions in flat-band systems. *Phys. Rev. B* **90**, 094506 (2014).

- Tsai, W. F., Fang, C., Yao, H. & Hu, J. Interaction-driven topological and nematic phases on the Lieb lattice. *New J. Phys.* **17**, 055016 (2015).
- Lieb, E. H. Two theorems on the Hubbard model. *Phys. Rev. Lett.* **62**, 1201–1204 (1989).
- Mielke, A. Exact ground states for the Hubbard model on the kagome lattice. *J. Phys. A* **25**, 4335–4345 (1992).
- Si, Q. & Steglich, F. Heavy fermions and quantum phase transitions. *Science* **329**, 1161–1166 (2010).
- Cao, Y. *et al.* Superlattice-induced insulating states and valley-protected orbits in twisted bilayer graphene. *Phys. Rev. Lett.* **117**, 116804 (2016).
- Suárez Morell, E., Correa, J. D., Vargas, P., Pacheco, M. & Barticevic, Z. Flat bands in slightly twisted bilayer graphene: tight-binding calculations. *Phys. Rev. B* **82**, 121407 (2010).
- Lopes dos Santos, J. M. B., Peres, N. M. R. & Castro Neto, A. H. Continuum model of the twisted graphene bilayer. *Phys. Rev. B* **86**, 155449 (2012).
- Fang, S. & Kaxiras, E. Electronic structure theory of weakly interacting bilayers. *Phys. Rev. B* **93**, 235153 (2016).
- Kim, K. *et al.* Tunable moiré bands and strong correlations in small-twist-angle bilayer graphene. *Proc. Natl Acad. Sci. USA* **114**, 3364–3369 (2017).
- Trambly de Laissardièrre, G., Mayou, D. & Magaud, L. Numerical studies of confined states in rotated bilayers of graphene. *Phys. Rev. B* **86**, 125413 (2012).
- Li, G. *et al.* Observation of van Hove singularities in twisted graphene layers. *Nat. Phys.* **6**, 109–113 (2010).
- Luican, A. *et al.* Single-layer behavior and its breakdown in twisted graphene layers. *Phys. Rev. Lett.* **106**, 126802 (2011).
- Brihuega, I. *et al.* Unraveling the intrinsic and robust nature of van Hove singularities in twisted bilayer graphene by scanning tunneling microscopy and theoretical analysis. *Phys. Rev. Lett.* **109**, 196802 (2012).
- Kim, K. *et al.* van der Waals heterostructures with high accuracy rotational alignment. *Nano Lett.* **16**, 1989–1995 (2016).
- Ashoori, R. C. *et al.* Single-electron capacitance spectroscopy of discrete quantum levels. *Phys. Rev. Lett.* **68**, 3088–3091 (1992).
- Novoselov, K. S. *et al.* Electric field effect in atomically thin carbon films. *Science* **306**, 666–669 (2004).
- Morozov, S. V. *et al.* Giant intrinsic carrier mobilities in graphene and its bilayer. *Phys. Rev. Lett.* **100**, 016602 (2008).
- Bolotin, K. I., Sikes, K. J., Hone, J., Stormer, H. L. & Kim, P. Temperature-dependent transport in suspended graphene. *Phys. Rev. Lett.* **101**, 096802 (2008).
- Mott, N. F. *Metal-Insulator Transitions* (Taylor and Francis, 1990).
- Imada, M., Fujimori, A. & Tokura, Y. Metal-insulator transitions. *Rev. Mod. Phys.* **70**, 1039–1263 (1998).
- Lee, P. A., Nagaosa, N. & Wen, X.-G. Doping a Mott insulator: physics of high-temperature superconductivity. *Rev. Mod. Phys.* **78**, 17–85 (2006).
- Misumi, K., Kaneko, T. & Ohta, Y. Mott transition and magnetism of the triangular-lattice Hubbard model with next-nearest-neighbor hopping. *Phys. Rev. B* **95**, 075124 (2017).
- Grüner, G. *Density Waves In Solids* (Westview Press, 2009).
- Balents, L. Spin liquids in frustrated magnets. *Nature* **464**, 199–208 (2010).

Acknowledgements We acknowledge discussions with L. Levitov, P. Lee, S. Todadri, B. I. Halperin, S. Carr, Z. Alpichshev, J. Y. Khoo and N. Staley. This work was primarily supported by the National Science Foundation (NSF; DMR-1405221) and the Gordon and Betty Moore Foundation's EPIQS Initiative through grant GBMF4541 for device fabrication, transport measurements and data analysis (Y.C., J.Y.L., J.D.S.-Y. and P.J.H.), with additional support from the NSS Program, Singapore (J.Y.L.). Capacitance work by R.C.A., A.D. and S.L.T. and theory work by S.F. was supported by the STC Center for Integrated Quantum Materials, NSF grant number DMR-1231319. Data analysis by V.F. was supported by AFOSR grant number FA9550-16-1-0382. K.W. and T.T. acknowledge support from the Elemental Strategy Initiative conducted by MEXT, Japan and JSPS KAKENHI grant numbers JP15K21722 and JP25106006. This work made use of the Materials Research Science and Engineering Center Shared Experimental Facilities supported by the NSF (DMR-0819762) and of Harvard's Center for Nanoscale Systems, supported by the NSF (ECS-0335765). E.K. acknowledges support by ARO MURI award W911NF-14-0247. R.C.A. acknowledges support by the Gordon and Betty Moore Foundation under grant number GBMF2931.

Author Contributions Y.C., J.Y.L. and J.D.S.-Y. fabricated the devices and performed transport measurements. Y.C. and V.F. performed data analysis. P.J.-H. supervised the project. S.F. and E.K. provided numerical calculations. S.L.T., A.D. and R.C.A. measured capacitance data. K.W. and T.T. provided hexagonal boron nitride devices. Y.C., V.F. and P.J.-H. wrote the paper with input from all authors.

Author Information Reprints and permissions information is available at www.nature.com/reprints. The authors declare no competing interests. Readers are welcome to comment on the online version of the paper. Publisher's note: Springer Nature remains neutral with regard to jurisdictional claims in published maps and institutional affiliations. Correspondence and requests for materials should be addressed to P.J.-H. (pjarillo@mit.edu).

METHODS

Sample preparation. Devices D1, D2 and D4 were fabricated using a modified 'tear and stack' technique^{13,17,22}. Monolayer graphene and hexagonal boron nitride (10–30-nm thick) were exfoliated on SiO₂/Si chips and examined with optical microscopy and atomic force microscopy. We used a poly(bisphenol A carbonate) (PC)/polydimethylsiloxane (PDMS) stack on a glass slide mounted on a micro-positioning stage to first pick up a hexagonal boron nitride flake at 90 °C. Then we used the van der Waals force between hexagonal boron nitride and graphene to tear a graphene flake at room temperature. The separated graphene pieces were rotated manually by an angle θ about 0.2°–0.3° larger than the desired twist angle and stacked together again, resulting in a precisely controlled TBG structure. The TBG was then encapsulated by picking up another hexagonal boron nitride flake on the bottom, and the entire stack was released onto a metal gate at 160 °C. The final device geometry was defined by electron-beam lithography and reactive ion etching. Device D3 was fabricated using a slightly different procedure, whereby independent graphene flakes were stacked together. The edges of the graphene flakes were aligned under an optical microscope to obtain small twist angles.

Measurements. Transport measurements were performed using a standard low-frequency lock-in amplifier with an excitation frequency of about 10–20 Hz and an excitation voltage of 100 μ V, in a He-3 cryostat. The current flowing through the device was amplified by a current pre-amplifier and then measured by the lock-in amplifier.

The capacitance was measured using a low-temperature balanced capacitance bridge²³. A schematic of the measurement circuit is shown in Extended Data Fig. 2a. The reference capacitance C_{ref} used in our experiment was approximately 40 fF, and the device geometrical capacitance was approximately 7 fF. The a.c. excitation voltage used in our measurements was 3 mV at $f = 150$ kHz.

Transport data in device D4. Transport measurements in devices D1 and D3 were performed in a two-probe configuration. Although it is generally advised to perform four-probe measurements in transport experiments, we found that the existence of multiple insulating states (the superlattice gaps at $\pm n_s$ and the half-filling states at $\pm n_s/2$) frequently led to noisy or negative longitudinal resistance R_{xx} signals, owing to the region in the device near the voltage probes becoming insulating at a slightly different carrier density. In our case, where we are mostly interested in insulating behaviours of the order of 100 k Ω to 1 M Ω , a contact resistance of at most a few kilo-ohms, which is typical in edge-contacted graphene devices, did not obscure the data³³. We therefore believe that the two-probe data presented here can be trusted and provide an accurate representation of the device characteristics.

In Extended Data Fig. 4b, c we show the measurements of the two-probe and four-probe conductances in device D4, which has a twist angle of $\theta = 1.16^\circ \pm 0.02^\circ$. Device D4 was measured in a Hall-bar configuration so that the contact resistance could be removed. In this particular device, neither the superlattice insulating states nor the half-filling states had very high impedance (probably owing to disorder or inhomogeneity), and so the previously described issues with four-probe measurements did not occur. The four-probe and two-probe measurements show essentially the same features, although some weak signals appear to be better resolved in the four-probe measurements.

In the four-probe data, we not only observe the half-filling states (± 2 electrons per moiré unit cell), but we also see evidence for odd-filling insulating phases at ± 3 electrons per moiré unit cell, as a weak reduction in the conductance curve. The existence of insulating behaviours at integer fillings of the flat bands other than ± 2 is expected in Mott-like insulators and lends further support to our claim that the correlated insulating behaviour originates from the on-site Coulomb interaction.

Hall measurement in device D4. We also measured device D4 in a Hall configuration (transverse resistance R_{xy}). In Extended Data Fig. 4d, e we show the low-field linear Hall coefficient $R_H = R_{xy}/B$ and the Hall density $n_H = -1/(eR_H)$ versus the gate-induced charge density n . In a uniformly gated single-carrier two-dimensional electronic gas, we expect that $n_H = n$. This is indeed what we measured in the density range $-1.3 \times 10^{12} \text{ cm}^{-2}$ to $1.3 \times 10^{12} \text{ cm}^{-2}$ at 0.3 K. However, near the half-filling states $n = \pm n_s/2$, the Hall density jumps abruptly from $n_H = n$ to a small value close to zero (but without changing its sign). Beyond half-filling, n_H follows $n_H = n \pm n_s/2$, a trend that is consistent with quasiparticles that are generated from the half-filling states. This 'resetting' effect of the Hall density disappears gradually as the temperature is raised from 0.3 K to 10 K, in agreement with the energy scale of the Mott-like states. At higher temperatures, the Hall density is linear with n but the slope is no longer one, which might be related to the thermal energy kT being close to the bandwidth, which could result in thermally excited carriers with opposite polarity reducing the net Hall effect.

In good correspondence with the quantum oscillation data shown in Fig. 3b, we see the behaviours of the new quasiparticles on only one side of the Mott-like state, for example, the side farther from the charge neutrality point; between the

charge neutrality point and the Mott-like state, we see an abrupt change from the typical large Fermi surface of the single-particle bands to a small Fermi surface of the new quasiparticles. This may result if the effective mass of the quasiparticles on one side of the Mott-like gap is considerably greater than the other side, so that the oscillation and Hall effect become difficult to observe very close to the metal–insulator transition.

Determining the twist angle. Accurate determination of the twist angles of the samples is of utmost importance in understanding the magic-angle physics. We used several independent methods to determine the twist angle from the transport data.

First, the superlattice density n_s , defined as the density that is required to fill one band in the superlattice, is related to the twist angle by

$$n_s = \frac{4}{A} \approx \frac{8\theta^2}{\sqrt{3}a^2} \quad (1)$$

where A is the unit-cell area and $a = 0.246$ nm is the lattice constant of graphene. At approximately $1^\circ < \theta < 3^\circ$, the superlattice densities $\pm n_s$ are associated with a pair of single-particle bandgaps at their corresponding Fermi energy^{13,34,35}. The measured density of the insulating states of the superlattice can therefore be used to estimate θ directly according to equation (1). Owing to localized states, an accurate value of n_s is difficult to pinpoint at zero magnetic field, and the estimated θ has an uncertainty of about 0.1°–0.2°. In Extended Data Fig. 7a–d we show the resistivity (resistance for magic-angle device D1) for four different TBG samples with twist angles of $\theta = 1.38^\circ, 1.08^\circ, 0.75^\circ$ and 0.65° . At $\theta = 1.38^\circ$ and 1.08° , the positions of the superlattice gaps provide an good estimate of θ . However, it has been noted¹⁷ that the apparent resistance peaks in the transport data may not correspond to n_s but instead to $2n_s$, when the twist angle is below about 0.9° – 1° . We observed a similar phenomenon when the twist angle was as small as 0.65° . This complicates the determination of twist angles, because of the ambiguity of whether the feature observed corresponds to n_s or $2n_s$, which can result in the twist angle being wrong by a factor of $\sqrt{2}$.

Second, we use the fact that each band edge of the mini-band structure has its own Landau levels^{13,34,36}. In Extended Data Fig. 7e we show the magneto-conductance data of device D1 (first derivative with respect to n). The Landau levels emanating from $n_s = (2.7 \pm 0.1) \times 10^{12} \text{ cm}^{-2}$ can be clearly seen, which translates to $\theta = 1.08^\circ \pm 0.02^\circ$ according to equation (1). Because the intersection points of the Landau levels can be determined relatively accurately (uncertainty of about $1 \times 10^{11} \text{ cm}^{-2}$), the twist angle can be determined with an uncertainty of about 0.02° near the first magic angle.

Third, the effect of applying strong magnetic fields such that the magnetic length becomes comparable with the unit-cell size is described by Hofstadter's butterfly model³⁷. In density space, this model is better captured by Wannier³⁸. In the Wannier diagram, the Landau levels are universally represented by $n/n_s = \nu\phi/\phi_0 + s$, where ϕ is the magnetic flux through a unit cell, ν is an integer, and $s = 0$ labels the main Landau fan, $s = \pm 1$ is the first satellite fan, and so on. Adjacent Landau fans intersect when $\phi/\phi_0 = 1/q$ or, equivalently, $1/B = qA/\phi_0$, where q is another integer. Therefore, in the experiments we expect to see Landau-level crossings at periodic intervals of $1/B$, with the periodicity proportional to the unit-cell area A . This effect has been observed in other two-dimensional superlattice systems and can be used to cross-check the twist angles extracted from other methods^{2–4}. In Extended Data Fig. 7f we show the magneto-transport data (first derivative with respect to n) of device D3 at high doping densities, plotted versus n and $1/B$. A periodic crossing of Landau levels is observed near $-9 \times 10^{12} \text{ cm}^{-2}$ with period $0.033 \pm 0.001 \text{ T}^{-1}$, which gives $A = (1.37 \pm 0.04) \times 10^{-12} \text{ cm}^2$ and $\theta = 1.12^\circ \pm 0.01^\circ$, compared to $\theta = 1.12^\circ \pm 0.02^\circ$ extracted using the previous method ($n_s = (2.9 \pm 0.1) \times 10^{12} \text{ cm}^{-2}$).

Estimating the Fermi velocity from capacitance data. The measured capacitance is the series sum of the geometric capacitance C_{geom} and the quantum capacitance C_q . The latter is directly proportional to the DOS in TBG. Therefore, by analysing the quantum capacitance C_q as a function of carrier density n , we can extract the dependence of DOS on n and subsequently deduce the Fermi velocity.

In the zero-temperature limit, the quantum capacitance is related to the DOS $D(E)$ by $C_q = e^2 D(E_F)$, where E_F is the Fermi energy. In a model system for TBG near charge neutrality that consists of massless Dirac fermions with Fermi velocity v_F and eight-fold degeneracy (spin, valley, layer), the DOS is^{39–41}

$$D(E_F) = \frac{4}{\pi} E_F (\hbar v_F)^2$$

Because $E_F = \hbar v_F k_F$ (where k_F is the Fermi wavevector) is related to the density n by

$$n = 8 \frac{1}{(2\pi)^2} \pi k_F^2 = \frac{2}{\pi} \frac{E_F^2}{(\hbar v_F)^2}, \quad E_F = \hbar v_F \sqrt{\frac{n\pi}{2}}$$

where the factor of 8 comes from the spin, valley and layer degeneracy, the quantum capacitance of the TBG is

$$C_q = e^2 \frac{2\sqrt{2}}{\sqrt{\pi} \hbar v_F} \sqrt{|n| + n_d} \quad (2)$$

Owing to disorder, the spatially averaged DOS at the Dirac point ($n = E_F = 0$) will not be absolutely zero. Therefore, a phenomenological disorder density of $n_d \approx 1 \times 10^{10} \text{ cm}^{-2}$ is added in the above expression³⁹.

The measured capacitance is then

$$\frac{1}{C} = \frac{1}{C_{\text{geom}}} + \frac{1}{C_q} \quad (3)$$

In Extended Data Fig. 2b, we show the measured capacitance near the Dirac point and fitting curves according to equations (2) and (3). C_{geom} is approximated by the d.c. gating capacitance $C_g \approx 7.5 \text{ fF}$. We find that using $v_F = 0.15 \times 10^6 \text{ m s}^{-1}$ and $n_d = 1 \times 10^{10} \text{ cm}^{-2}$ gives a reasonable fit to the data measured at both 0.3 K and 2 K.

The fitting for v_F is sensitive to the value used for C_{geom} . For example, using a C_{geom} value 30% larger than the value that we used above, we find a Fermi velocity of $v_F = 0.10 \times 10^6 \text{ m s}^{-1}$. Similarly, using a value 15% smaller than the said value we find $v_F = 0.20 \times 10^6 \text{ m s}^{-1}$. Nonetheless, the analysis presented here suffices to demonstrate that the Fermi velocity is indeed reduced greatly in the capacitance device D2. The slightly larger Fermi velocity compared to that measured in the transport device D1 ($v_F = 0.04 \times 10^6 \text{ m s}^{-1}$) can be attributed to the slightly larger twist angle of device D2 ($\theta = 1.10^\circ$), which might be farther from the first magic angle $\theta_{\text{magic}}^{(1)} \approx 1.05^\circ$.

Error bars. The error bars in the inset of Fig. 2a are computed using the following criteria: for the transport devices D1, D3 and D4, the endpoints of the error bars correspond to the points at which the conductance rises to 10% of the peak value on that side; for the capacitance device D2, because the peaks are very sharp (see Fig. 3a), the error bar corresponds to the width of the entire peak in the loss tangent data.

Quantum oscillations and extracting m^* . We performed magneto-transport measurements in device D1 from 0.3 K to 10 K. At each gate voltage, a polynomial background of resistance in B was first removed, and then the oscillation frequency and the effective mass was analysed. Examples of the Shubnikov–de Haas oscillations and their temperature dependences at a few representative gate voltages are shown in Extended Data Fig. 3a–c. The temperature dependence of the most prominent peak is fitted with the Lifshitz–Kosevich formula applied to the resistance:

$$\Delta R \propto \frac{\chi}{\sinh(\chi)}, \quad \chi = \frac{2\pi^2 k T m^*}{\hbar e B} \quad (4)$$

where ΔR is the change in resistance and the cyclotron mass m^* is extracted from the fitting (examples shown in Extended Data Fig. 3d). Within the flat bands, the quantum oscillations universally disappear at around 10 K except very close to the Dirac point, consistent with the large electron mass and greatly reduced Fermi velocity near the first magic angle.

The full magneto-conductance map measured in device D1 at 0.3 K is shown in Extended Data Fig. 5c. At first glance, it may seem that the Landau levels that emanate from the Dirac point ‘penetrate’ the half-filling states and continue towards the band edges. However, this is not the case. In Extended Data Fig. 3e, f we show the same data but plotted versus $1/B$ instead of B . Here it can be seen that at densities beyond the half-filling states, the oscillations clearly do not converge at the Dirac point, instead converging at the half-filling states. The oscillation frequencies extracted from these data are plotted in Fig. 3b.

Band structure of TBG near magic angles. The general evolution of the band structure of TBG above the first magic angle has been described previously^{6,14–16,18,34,35}. The low-energy band structure consists of two Dirac cones (each is four-fold-degenerate owing to valley and spin), with a renormalized Fermi velocity of

$$v_F(\theta) = v_0 \frac{1 - 3\alpha^2}{1 + 6\alpha^2}$$

where $\alpha = w/(\hbar v_0 k_\theta)$ is the dimensionless interlayer hopping amplitude (w and v_0 are the interlayer hopping energy and original Fermi velocity in graphene, $k_\theta \approx G_K \theta$ is the interlayer momentum difference and G_K is the wave number at the corner of the Brillouin zone in graphene)^{6,15}. When $\alpha \ll 1$, $v_F(\theta)$ is approximately $v_0(1 - 9\alpha^2)$. $v_F(\theta)$ passes through zero at $\alpha = 1/\sqrt{3}$, which defines the first magic angle $\theta_{\text{magic}}^{(1)}$. However, to our knowledge, the detailed evolution of the band structure near magic angles has not been addressed previously. Specifically, we seek to

determine how the associated winding number evolves as the Fermi velocity at the Dirac points changes sign. Close to a generic Dirac point, the effective two-band Hamiltonian can be written as⁴²

$$\mathcal{H}(\mathbf{k}) = \hbar v_F(\theta) \boldsymbol{\sigma} \cdot \mathbf{k} + \mathcal{O}(k^2) = \begin{bmatrix} \mathcal{O}(k^2) & \hbar v_F(\theta) k^\dagger + \mathcal{O}(k^2) \\ \hbar v_F(\theta) k + \mathcal{O}(k^2) & \mathcal{O}(k^2) \end{bmatrix}$$

in which $\mathbf{k} = (k_x, k_y)$, $k = k_x + ik_y$ and $\boldsymbol{\sigma} = (\sigma_x, \sigma_y)$ is the vector of the Pauli matrices. As $v_F(\theta) \rightarrow 0$ near the first magic angle, the terms that are linear in k vanish and the dispersion is dominated by the next-leading-order, k^2 terms. A simple form for the k^2 term is

$$\mathcal{H}(\mathbf{k}) = \begin{bmatrix} 0 & \hbar v_F(\theta) k^\dagger + \frac{\hbar^2}{2m} k^2 \\ \hbar v_F(\theta) k + \frac{\hbar^2}{2m} (k^\dagger)^2 & 0 \end{bmatrix} \quad (5)$$

in which m is a parameter with the dimension of mass. This Hamiltonian describes the low-energy band dispersion of monolayer graphene with third-nearest-neighbour hopping and of bilayer graphene with Bernal stacking and trigonal warping^{42–46}. The eigenvalues of this Hamiltonian are

$$E_{\pm}(\mathbf{k}) = \pm \sqrt{\left[\hbar v_F k_x + \frac{\hbar^2}{2m} (k_x^2 - k_y^2) \right]^2 + \left[\hbar v_F k_y - \frac{\hbar^2}{m} k_x k_y \right]^2} \quad (6)$$

The evolution of the dispersion described by equation (6) with varying v_F and a constant $m = 0.5$ is shown in Extended Data Fig. 1a–f. The winding number associated with a Dirac point is defined by

$$w = \frac{i}{2\pi} \oint_C \langle \mathbf{k} | \nabla_{\mathbf{k}} | \mathbf{k} \rangle d\mathbf{k}$$

where C is a loop around the Dirac point. The winding number follows a conservation law when the motion and merging of Dirac points are considered⁴². The winding number of the upper band ($E_+(\mathbf{k})$) at each touching point in the upper band is labelled in Extended Data Fig. 1a–f.

As $v_F \rightarrow 0$ there exist three additional Dirac points with opposite winding number (-1) to the main Dirac point ($+1$). Therefore, at $v_F = 0$, when all four Dirac points merge, the winding number is -2 because the total winding number cannot change.

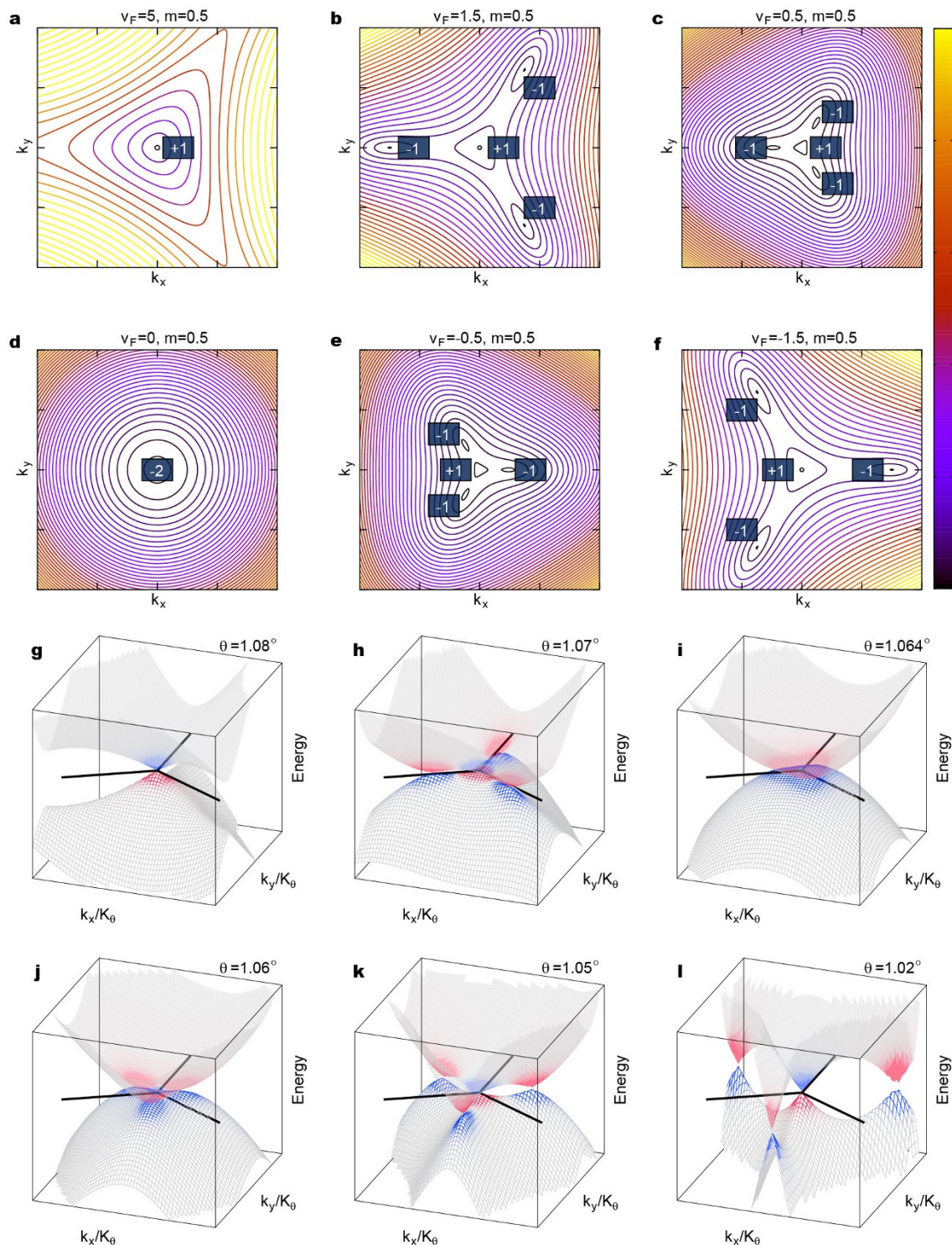
The simple Hamiltonian form in equation (5) is an educated guess. We performed numerical calculations of the winding number using the continuum model for TBG^{6,15} and the numerical method in ref. 47. The results are summarized in Extended Data Fig. 1g–l. We find that near the first magic angle of the model used, $\theta_{\text{magic}}^{(1)} = 1.064^\circ$, the behaviour described in Extended Data Fig. 1a–f is exactly what happens at each corner of the mini Brillouin zone. The complication that arises when we consider the entire mini Brillouin zone is that, for a given valley (of the original graphene Brillouin zone, such as K), the two inequivalent corners of the mini Brillouin zone have the same winding number because they are the hybridized result of the same valley (K) of opposite layers (see Fig. 1d). Global time-reversal symmetry is preserved by mapping to the other valley (K'). Therefore, for a given valley K , when the twist angle is reduced from large angles, at which the winding numbers of the two corners are $(+1, +1)$, to the first magic angle, at which the winding numbers are $(-2, -2)$, a net winding number change of $\Delta w = 6$ occurs between the two lowest-energy bands. Further theoretical work is necessary to elucidate the physics behind this winding number evolution near the first magic angle.

In summary, we show that at exactly the first magic angle the Dirac point at each corner of the mini Brillouin zone (K_s and K'_s) becomes a parabolic band touching with a winding number of -2 , similarly to bilayer graphene with Bernal stacking except that the two corners have the same winding number. The calculation that corresponds to the first magic angle in Extended Data Fig. 1i can be fitted to a paraboloid, which yields an effective mass of $1.1 m_e$. This value can be viewed as the asymptotic limit of the effective mass near the charge neutrality point as $v_F \rightarrow 0$. **DOS in magic-angle TBG.** Despite our simplistic representation of the DOS in the flat bands of magic-angle TBG (Fig. 4d–f), the actual single-particle DOS profile of magic-angle TBG is more complex, with multiple van Hove singularities. In Extended Data Fig. 6 we show the DOS versus energy calculated using a continuum model⁶ for $\theta = 1.08^\circ$.

Data availability. The data that support the findings of this study are available from the corresponding author on reasonable request.

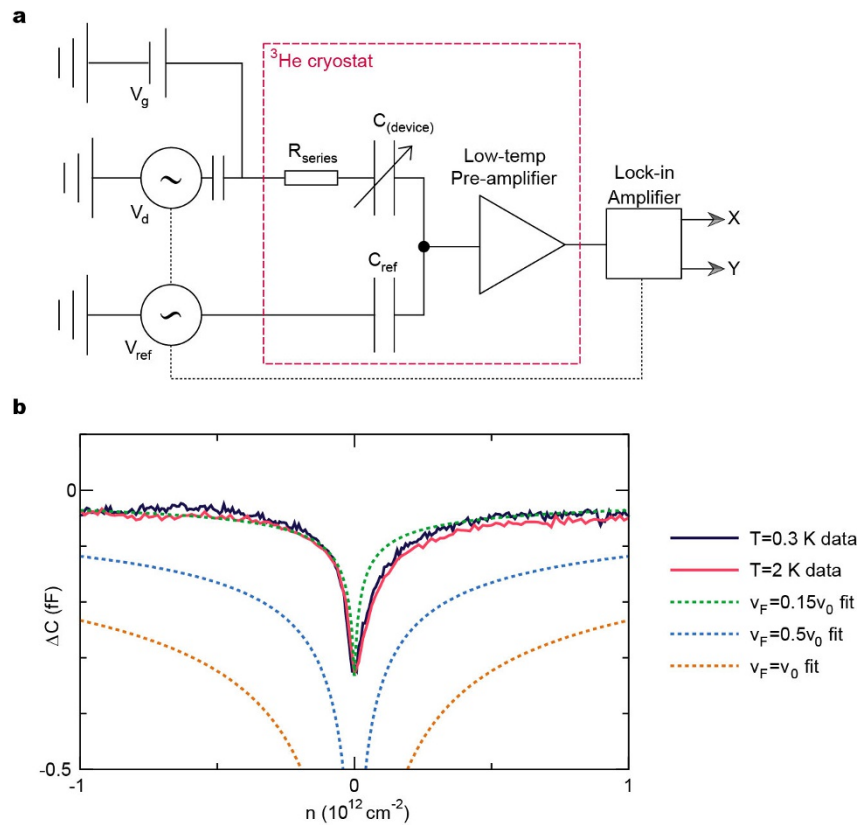
33. Wang, L. *et al.* One-dimensional electrical contact to a two-dimensional material. *Science* **342**, 614–617 (2013).

34. Moon, P. & Koshino, M. Energy spectrum and quantum Hall effect in twisted bilayer graphene. *Phys. Rev. B* **85**, 195458 (2012).
35. Nam, N. N. T. & Koshino, M. Lattice relaxation and energy band modulation in twisted bilayer graphenes. *Phys. Rev. B* **96**, 075311 (2017).
36. Kim, Y. *et al.* Charge inversion and topological phase transition at a twist angle induced van Hove singularity of bilayer graphene. *Nano Lett.* **16**, 5053–5059 (2016).
37. Hofstadter, D. R. Energy levels and wave functions of Bloch electrons in rational and irrational magnetic fields. *Phys. Rev. B* **14**, 2239–2249 (1976).
38. Wannier, G. H., A result not dependent on rationality for Bloch electrons in a magnetic field. *Phys. Status Solidi b* **88**, 757–765 (1978).
39. Xia, J., Chen, F., Li, J. & Tao, N. Measurement of the quantum capacitance of graphene. *Nat. Nanotechnol.* **4**, 505–509 (2009).
40. Fang, T., Aniruddha, K., Xing, H. & Jena, D. Carrier statistics and quantum capacitance of graphene sheets and ribbons. *Appl. Phys. Lett.* **91**, 092109 (2007).
41. Wallace, P. R. The band theory of graphite. *Phys. Rev.* **71**, 622–634 (1947).
42. Goerbig, M. & Montambaux, G. in *Dirac Matter* (eds Duplantier, B. *et al.*) 25–53 (Springer, 2017).
43. Bena, C. & Simon, L. Dirac point metamorphosis from third-neighbor couplings in graphene and related materials. *Phys. Rev. B* **83**, 115404 (2011).
44. Montambaux, G. An equivalence between monolayer and bilayer honeycomb lattices. *Eur. Phys. J. B* **85**, 375 (2012).
45. McCann, E. & Koshino, M. The electronic properties of bilayer graphene. *Rep. Prog. Phys.* **76**, 056503 (2013).
46. McCann, E. & Fal'ko, V. I. Landau-level degeneracy and quantum Hall effect in a graphite bilayer. *Phys. Rev. Lett.* **96**, 086805 (2006).
47. Fukui, T., Hatsugi, Y. & Suzuki, H. Chern numbers in discretized Brillouin zone: efficient method of computing (spin) Hall conductances. *J. Phys. Soc. Jpn* **74**, 1674–1677 (2005).



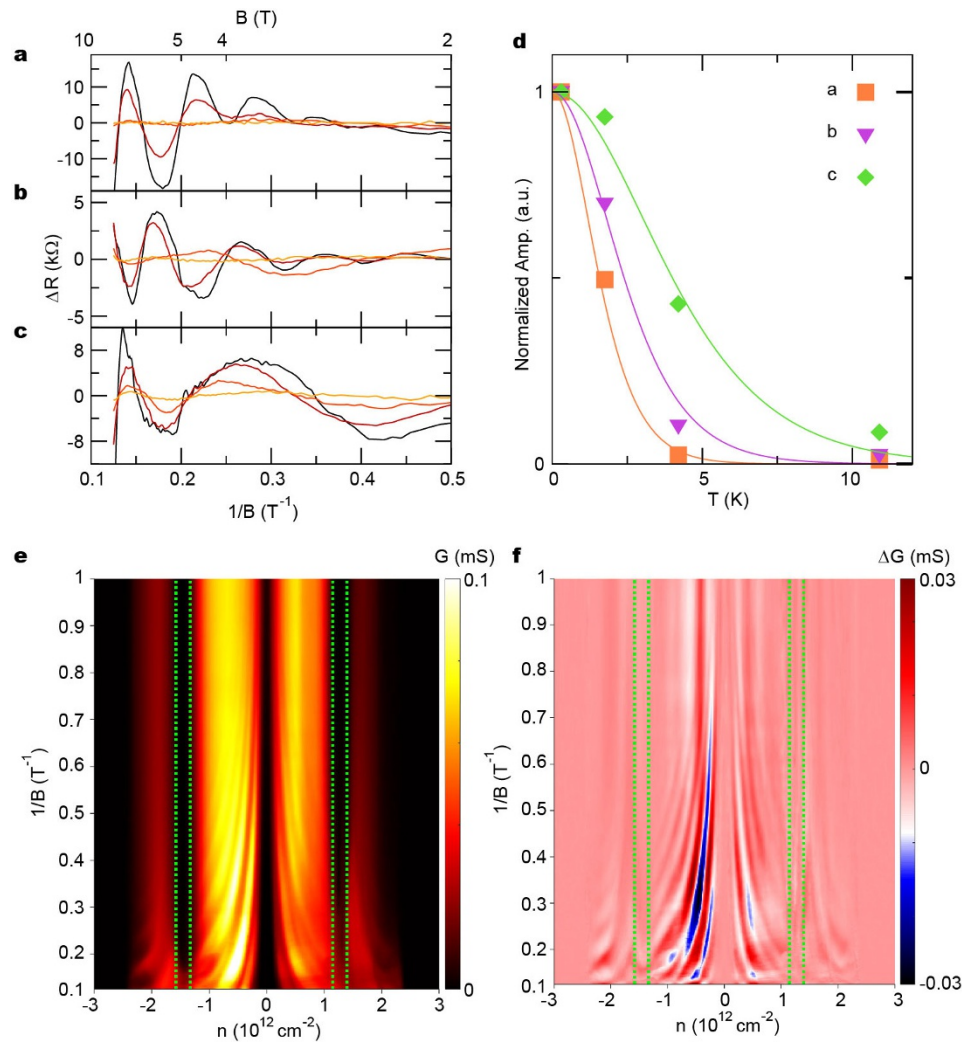
Extended Data Figure 1 | Evolution of the low-energy band structure of TBG near the magic angle. a–f, E_+ dispersion as in equation (6) for different v_F and fixed $m = 0.5$. The k_x and k_y range in the figures is $[-2, 2]$ and the colour scale (on the right side of the figures) for the dimensionless energy axis is 0 to 10 from bottom to top. The associated winding number of each touching point is labelled. g–l, The evolution of the low-energy band structure of TBG near the first magic angle $\theta_{\text{magic}}^{(1)} = 1.064^\circ$ in the model. The colour shows the hotspots of the Berry curvature at the

touching point of each band. The energy axis spans an extremely small range of $[-50, 50] \mu\text{eV}$. The momentum axes are measured by $k_\theta \approx K\theta$ and the range for both k_x/K_θ and k_y/K_θ is $[-0.1, 0.1]$. The centre of the momentum space is the K_s point of the mini Brillouin zone (see Fig. 1d), and the thick lines denotes the K_s - M_s - K'_s directions (there are three inequivalent ones). All results are shown for the K-valley continuum description of TBG⁶.



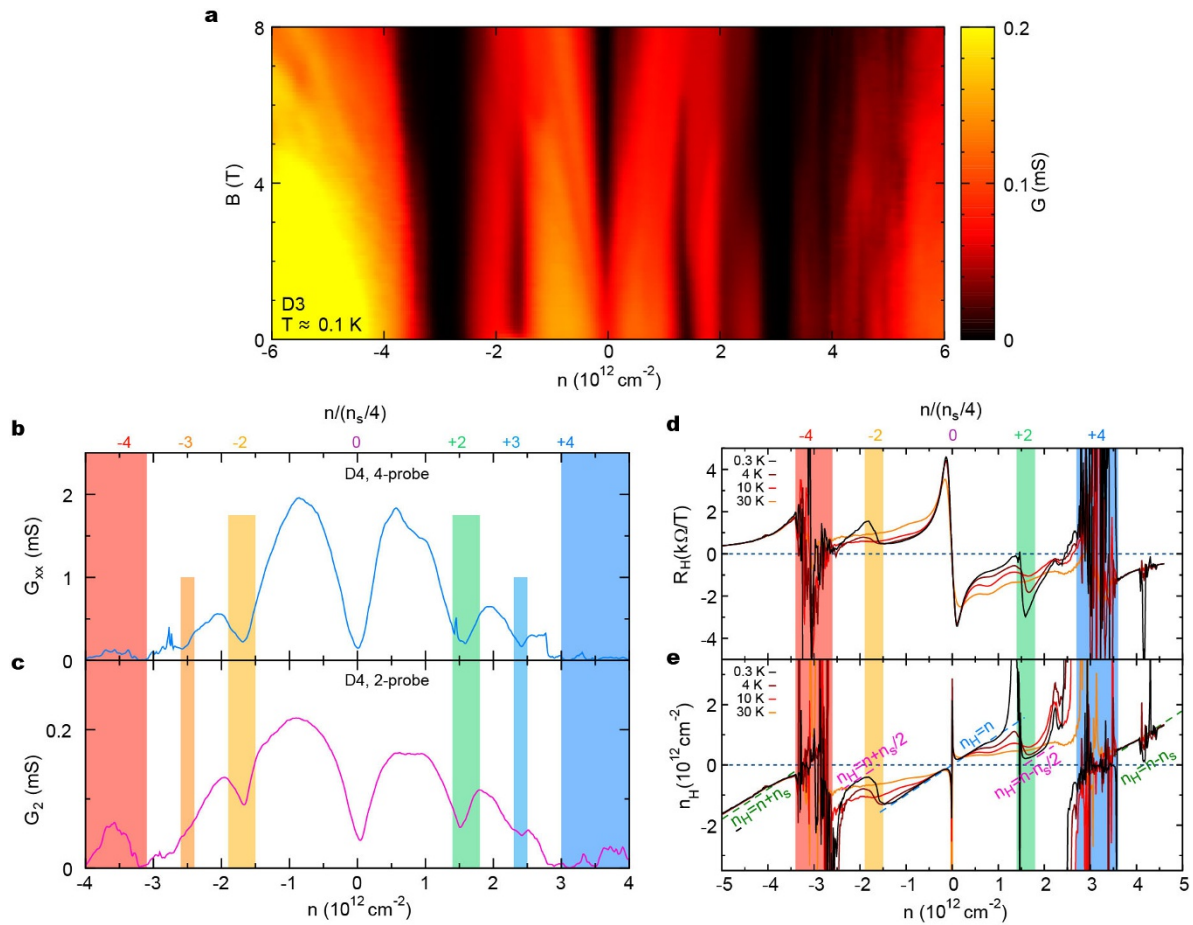
Extended Data Figure 2 | Capacitance measurement set-up and extraction of the Fermi velocity. **a**, Schematic of the low-temperature capacitance bridge. The X and Y outputs from the lock-in amplifier refer to the in-phase and out-of-phase components, respectively. $C_{\text{(device)}}$ and R_{series} are the capacitance and resistance of the sample. V_g is the d.c. gate voltage, V_d is the excitation voltage, V_{ref} is the reference voltage and C_{ref} is

the reference capacitance. All connections into and out of the cryostat are made with coaxial cables. **b**, Capacitance ΔC of device D2 near the charge neutrality point, and fitting curves according to equations (4) and (5) with different Fermi velocities. $v_0 = 10^6 \text{ m s}^{-1}$ is the Fermi velocity in pristine graphene.



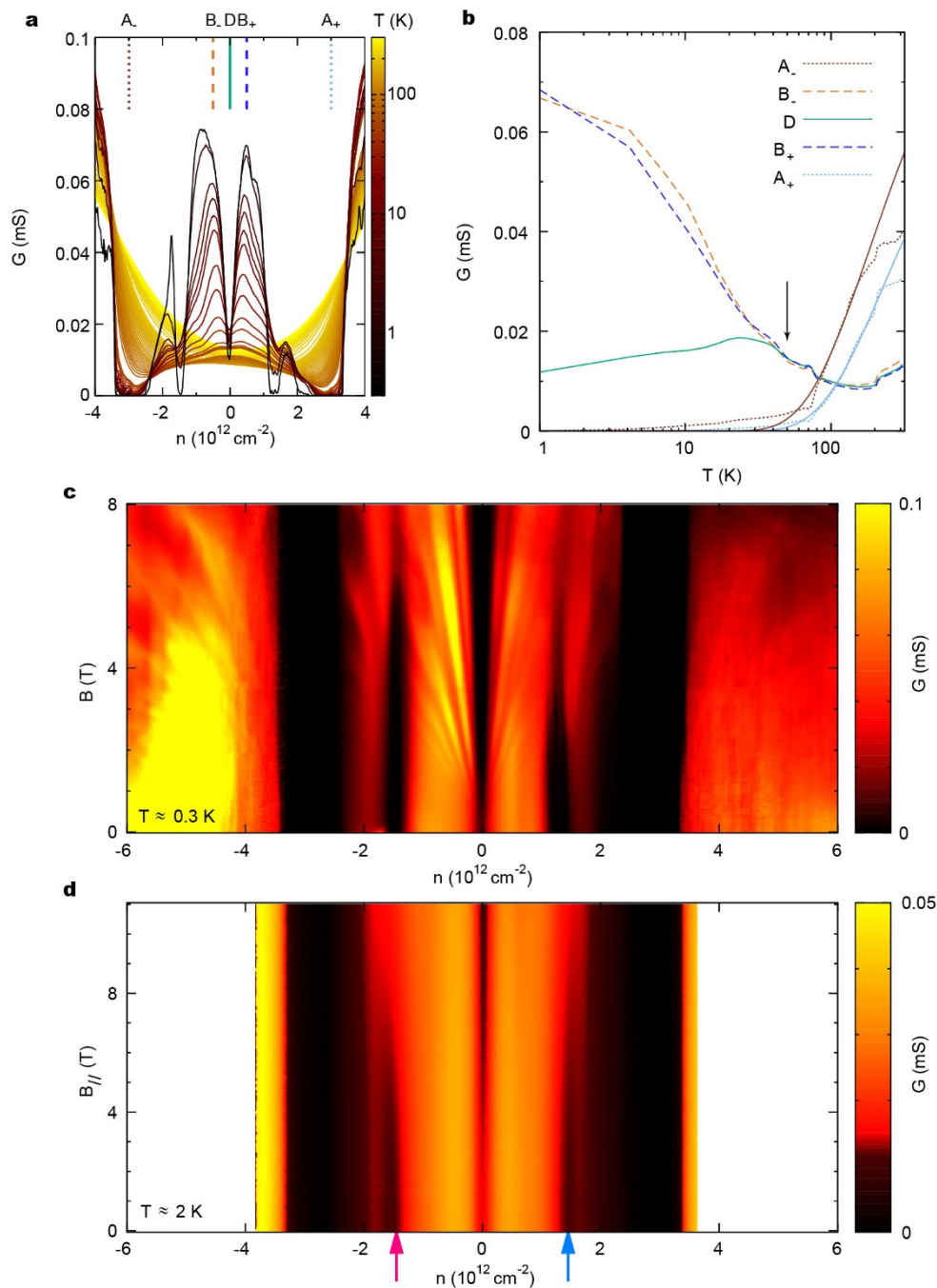
Extended Data Figure 3 | Quantum oscillations and extraction of the effective mass. **a–c**, Temperature-dependent magneto-resistance ΔR of device D1 at gate-voltage-induced carrier densities of $n = -2.08 \times 10^{12} \text{ cm}^{-2}$ (**a**), $n = -1.00 \times 10^{12} \text{ cm}^{-2}$ (**b**) and $n = 0.19 \times 10^{12} \text{ cm}^{-2}$ (**c**). The temperatures are, from dark to bright, 0.3 K, 1.7 K, 4.2 K and 10.7 K. **d**, Oscillation amplitudes of the most prominent peaks in **a–c**. The curves are fitted according to the Lifshitz–Kosevich formula

(equation (4)). **e**, Magneto-conductance G of device D1 (measured at 0.3 K) plotted versus n and $1/B$. **f**, The same data with a polynomial background in B removed for each density. The green boxes denote the range of densities for the half-filling states. At densities beyond the half-filling states, the oscillations do not converge at the Dirac point, but instead at the half-filling states.



Extended Data Figure 4 | Supplementary transport data in devices D3 and D4. **a**, Magneto-conductance G in device D3 ($\theta = 1.12^\circ$) versus n and B . The primary features at the superlattice gaps $\pm n_s$ and the half-filling states $\pm n_s/2$ are essentially identical to those for device D1. **b**, **c**, Four-probe (**b**; G_{xx}) and two-probe (**c**; G_2) conductance measured in device D4 ($\theta = 1.16^\circ$) at 0.3 K. The coloured vertical bars and the corresponding numbers indicate the associated integer filling inside each unit cell of the moiré pattern. As well as the half-filling states (± 2), we also observe weak

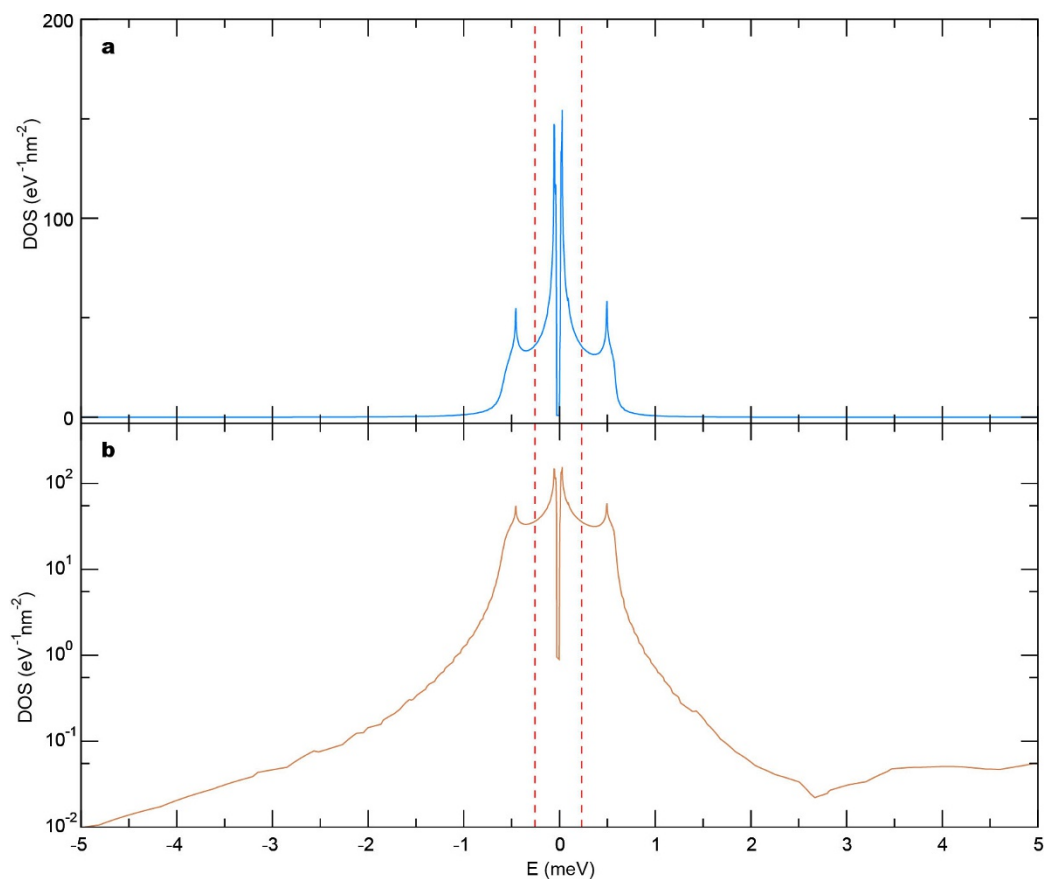
drops in the four-probe conductivity that point to three-quarter-filling states at ± 3 . **d**, **e**, Hall measurement in device D4 at various temperatures: the Hall coefficients R_H (**d**) and the Hall density $n_H = -1/(eR_H)$ (**e**). The coloured vertical bars and the corresponding numbers are as in **b** and **c**. The x axis is the gate-induced total charge density n , whereas the Hall density n_H and its sign indicate the number density and characteristic (electron-like or hole-like) curve of the carriers being transported.



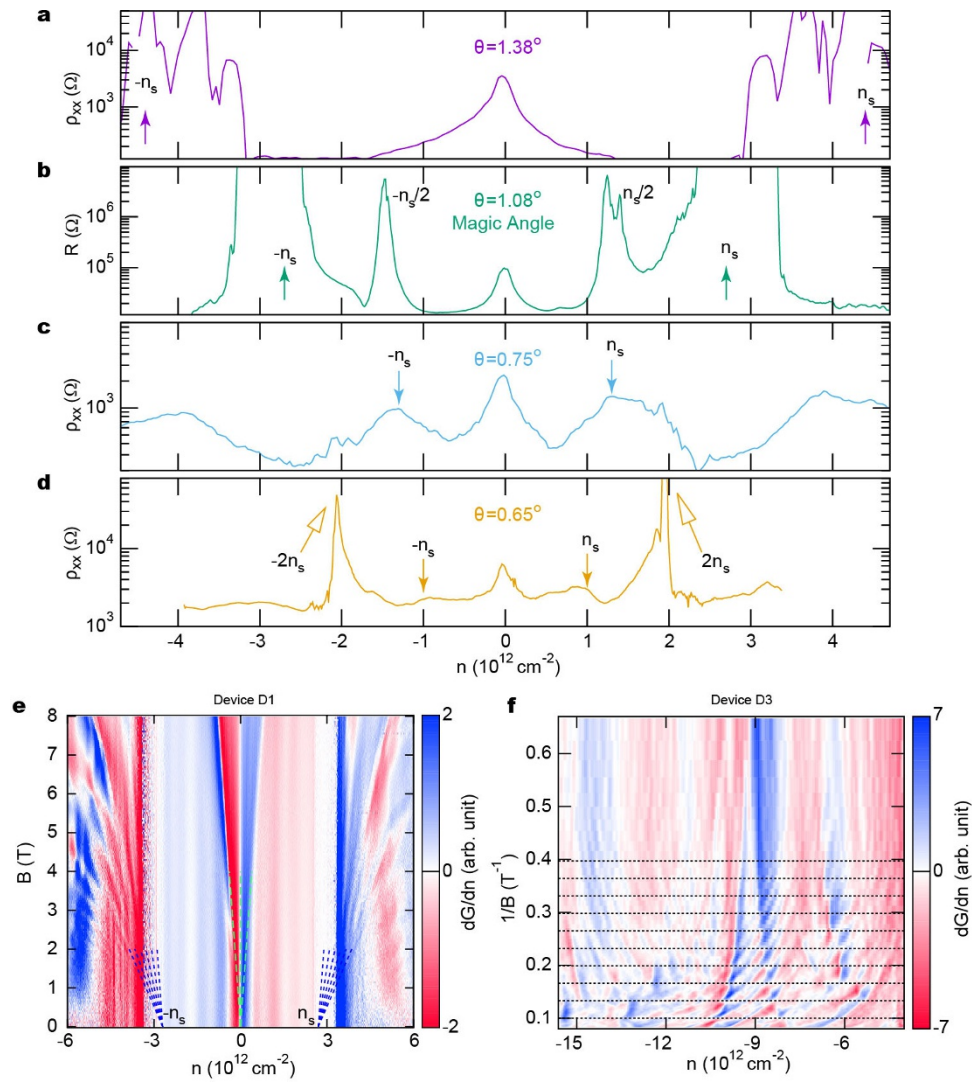
Extended Data Figure 5 | Supplementary transport data in device D1.

a, Temperature dependence of the conductance G of device D1 from 0.3 K to 300 K. **b**, The conductance versus temperature at five characteristic carrier densities, labelled A_{\pm} (superlattice gaps), B_{\pm} (above and below the Dirac point) and D (the Dirac point) in **a**. The arrow denotes the temperature above which the conductances at B_{\pm} merge with that of D . The solid lines accompanying the A_{\pm} traces are Arrhenius fits to the data. The thermal activation gaps of the superlattice insulating states at A_{\pm} can be obtained by fitting the temperature dependence of the conductance at these densities. See ref. 13 for a detailed discussion about the superlattice gaps in non-magic-angle devices. The fit to the Arrhenius formula $\exp[-\Delta/(2kT)]$ yields $\Delta_- = 32 \text{ meV}$ for the A_- gap and $\Delta_+ = 40 \text{ meV}$ for the A_+ gap. For comparison, the same gaps measured in $\theta = 1.8^\circ$ TBG are

slightly larger, $\Delta_- = 50 \text{ meV}$ and $\Delta_+ = 60 \text{ meV}$ for the gaps at negative and positive densities, respectively¹³. **c**, Magneto-conductance in device D1 as a function of gate-induced charge density n and perpendicular magnetic field B_{\perp} . **d**, Magneto-conductance in device D1 measured as a function of n and in-plane magnetic field B_{\parallel} . The in-plane measurement is made at a higher temperature of about 2 K. Combined with the degradation of the sample quality that resulted from the thermal cycling that was necessary to change the field orientation, the half-filling states are not as well developed as in the previous measurements. However, the gradual suppression of the half-filling states is still unambiguously observed when B_{\parallel} is above about 6 T, slightly higher but similar to the approximately 4–6-T threshold for the perpendicular field (see **c** and Fig. 4a, b). The red and blue arrows point to the p-side and n-side half-filling states, respectively.



Extended Data Figure 6 | DOS in magic-angle TBG. **a, b**, Single-particle DOS in TBG at $\theta = 1.08^\circ$, on linear (**a**) and logarithmic (**b**) scales. The red dashed lines denote the energy at which the lower and upper flat bands are half-filled. The results are obtained numerically using a continuum model⁶.



Extended Data Figure 7 | Determining the twist angle. **a–d**, Resistivity ρ_{xx} (resistance R for the $\theta = 1.08^\circ$ device) measurements for four samples with different twist angles: $\theta = 1.38^\circ$ (**a**), $\theta = 1.08^\circ$ (**b**), $\theta = 0.75^\circ$ (**c**) and $\theta = 0.65^\circ$ (**d**). The filled arrows highlight superlattice features at $\pm n_s$ and open arrows highlight $\pm 2n_s$ features that may correspond to features reported in ref. 17. So far, we have observed the half-filling states only in devices that have twist angles within 0.1° of the first magic angle. **e**, Magneto-conductance data (derivative with respect to n ; dG/dn) of

device D1 ($\theta = 1.08^\circ$) measured at 4 K. The dashed lines label the main (green) and satellite (blue) Landau fans. From the convergence point of the blue fans, we can accurately determine the superlattice density n_s and thus θ , with an uncertainty of about 0.02° . **f**, Hofstadter's oscillation manifested as periodic crossings of Landau levels in $1/B$. Data shown is the magneto-conductance (derivative with respect to n ; dG/dn) of device D3 ($\theta = 1.12^\circ$). The horizontal lines have a uniform spacing of $0.033 \pm 0.001 \text{ T}^{-1}$, which corresponds to $\theta = 1.12^\circ \pm 0.01^\circ$.